NeuroImage: Clinical 27 (2020) 102340

Contents lists available at ScienceDirect

NeuroImage: Clinical

journal homepage: www.elsevier.com/locate/ynicl

Post-mortem 7 Tesla MRI detection of white matter hyperintensities: A multidisciplinary voxel-wise comparison of imaging and histological correlates

Austyn D. Roseborough[a], Kristopher D. Langdon[b], Robert Hammond[b], Lauren E. Cipriano[c], Stephen H. Pasternak[d], Shawn N. Whitehead[a,*,1], Ali R. Khan[e,1]

[a] Department of Anatomy and Cell Biology, The Schulich School of Medicine and Dentistry, The University of Western Ontario, London, Ontario, Canada
[b] Department of Pathology and Laboratory Medicine, The Schulich School of Medicine and Dentistry, The University of Western Ontario, London, Ontario, Canada
[c] Ivey Business School and Department of Epidemiology and Biostatistics, The University of Western Ontario, London, Ontario, Canada
[d] Department of Clinical Neurological Sciences, Robarts Research Institute, The Schulich School of Medicine and Dentistry, The University of Western Ontario, London, Ontario, Canada
[e] Department of Medical Biophysics, The Schulich School of Medicine and Dentistry, The University of Western Ontario, London, Ontario, Canada

ARTICLE INFO

Keywords:
White Matter Hyperintensities
Ultra High Field MRI
Small Vessel Disease

ABSTRACT

White matter hyperintensities (WMH) occur in normal aging and across diagnostic categories of neurodegeneration. Ultra-high field imaging (UHF) MRI machines offer the potential to improve our understanding of WMH. Post-mortem imaging using UHF magnetic resonance imaging (MRI) is a useful way of assessing WMH, however, the responsiveness of UHF-MRI to pathological changes within the white matter has not been characterized. In this study we report post-mortem MRI sequences of white matter hyperintensities in normal aging, Alzheimer's disease, and cerebrovascular disease. Seven Tesla post-mortem MRI reliably detected periventricular WMH using both FLAIR and T2 sequences and reflects underlying pathology of myelin and axon density despite prolonged fixation time. Co-registration of histological images to MRI allowed for direct voxel- wise comparison of imaging findings and pathological changes. Myelin content and cerebrovascular pathology were the most significant predictors of MRI white matter intensity as revealed by linear mixed models. Future work investigating the utility of UHF- MRI in studying cell-specific changes within WMH is required to better understand radio-pathologic correlations.

1. Introduction

White matter hyperintensities (WMH) are markers of aging and are often referred to as clinical markers of cerebral small vessel disease (SVD), although their pathophysiology remains poorly defined (Wardlaw et al., 2013). SVD can result in hypoperfusion and chronic ischemia of the white matter that is believed to contribute to development of microbleeds, enlarged perivascular spaces, lacunar infarcts and WMH (Wardlaw et al., 2013). Clinically, these markers of SVD are identified using Magnetic Resonance Imaging (MRI). WMH specifically appear as hyperintense regions on T2 and Fluid Attenuated Inversion Recovery (FLAIR) weighted sequences (Wardlaw et al., 2013). Due to increasing midlife occurrence of WMH, with estimates of greater than 50% prevalence in individuals over the age of 40 (Wen et al., 2009), an understanding of the pathological mechanisms underlying WMH is required (Wen et al., 2008). WMH appear in normal aging and vascular dementia, and have been described as a core feature of Alzheimer's Disease (AD) (Lee et al., 2016). WMH have been associated with cognitive decline (Breteler et al., 1994; Deary et al., 2003), specifically affecting executive functions (Debette and Markus, 2010; Jacobs et al., 2012). Moreover, recent *meta*-analyses have suggested that WMH are associated with an increased risk of all dementias (Bos et al., 2018; Debette and Markus, 2010). In addition to dementing illnesses, WMH have also been associated with cerebrovascular disease (CVD) including both overt and clinically silent strokes. Despite their clinical relevance, the cause and development of WMH is not well understood but reports

Abbreviations: AD, Alzheimer s Dementia; CVD, Cerebrovascular Disease; FLAIR, Fluid Attenuated Inversion Recovery; MRI, Magnetic Resonance Imaging; SVD, Small Vessel Disease; UHF, Ultra High Field; WMH, white matter hyperintensities

* Corresponding author.
E-mail address: shawn.whitehead@schulich.uwo.ca (S.N. Whitehead).

[1] Both authors contributed equally.

https://doi.org/10.1016/j.nicl.2020.102340
Received 28 January 2020; Received in revised form 2 June 2020; Accepted 2 July 2020
Available online 06 July 2020

of underlying pathology note demyelination, rarefaction, edema and gliosis (Fazekas et al., 1993). While these features of WMH are difficult to study prior to pathological analysis, the ability of neuroimaging to reflect these pathological changes is an important feature that reflects much of the focus of *in vivo* studies of WMH.

The comorbidity of WMH with many other neurological conditions makes them an ideal target to study, especially if common pathological changes are occurring across diagnostic categories. Studies reporting WMH in AD reflect a more severe expression of the same pathological changes as WMH in normal aging (Scheltens et al., 1995). Others report that WMH in normal aging primarily involve myelin loss, while WMH in AD may also be driven by axonal loss and the negative impact of chronic microglial activation (Gouw et al., 2008a). Despite these potential differences in underlying pathophysiology, at lower field strengths WMH across diagnostic categories can appear homologous on qualitative and quantitative MR sequences such as diffusion tensor imaging (DTI) in healthy aging and AD (Swardfager et al., 2017). It is not well understood whether current advancements in MR imaging resolution will enable distinction between heterogeneous histopathological features of WMH (Gouw et al., 2011) and improved identification of subclinical tissue abnormalities. Most clinical studies use whole brain imaging to estimate WMH burden, however this can be limited by imaging resolution that may not detect the smallest WMH often millimeters in size. Improvements in field strength and image resolution may allow for more sensitive detection of pathological features unique to WMH occurring amongst various neurological disease states.

A current limitation in the study of WMH is the difficulty correlating MRI characteristics and neuropathology due to the usually long interval between MRI acquisition and time of death. Post-mortem MRI is a valuable approach to detect WMH and other markers of SVD; and can be performed on long-term fixed tissue (Awad et al., 1986; Braffman et al., 1988; Grafton et al., 1991; Grinberg et al., 2009; Nagara et al., 1987; van den Hauwe et al., 1995). It allows for direct comparison of WMH with pathological changes, both temporally and anatomically when paired with digitized histological data (Grinberg et al., 2009; Murray et al., 2012). Previous work suggests that post-mortem MRI is accurate for visualizing WMH with severe underlying pathological changes but can underestimate lesion size when the pathological changes are subtle (Bronge et al., 2002; Fernando et al., 2004). Ultra high-field (UHF) strength MRI scanners potentially offer the opportunity for improved detection of WMH. However, there is a need to understand the ability of higher field strengths to detect WMH utilizing a variety of qualitative and quantitative sequences (Black et al., 2009). This may be especially important when comparing longitudinal imaging collected at a variety of field strengths, with different sensitivities to white matter loss. Recent work, using lower field strengths, suggests that qualitative sequences of normal-appearing white matter may in fact show abnormalities when examined histologically (Muñoz Maniega et al., 2016). The scope of white matter pathology is not limited to the borders visualized on MRI and may reflect an extension of SVD throughout the subcortical white matter (Muñoz Maniega et al., 2016; Shi and Wardlaw, 2016). It is therefore the aim of this study to characterize the accuracy of qualitative 7 T post-mortem MRI sequences in delineating the histological features of both WMH and normal-appearing white matter. This is the first study, to our knowledge, that compares the histological features of post-mortem WMH using UHF-MRI in patients with an array of confirmed neuropathological diagnoses. Results show that post-mortem FLAIR, T2 and quantitative T1 are associated with histological evidence of white matter rarefaction. Using a voxel-wise approach to generate mixed models of FLAIR intensity, results show that UHF post-mortem MRI is a valid tool for the assessment of white matter rarefaction. Post-mortem intensity is sensitive to changes in myelin content in a voxel-wise manner and further influenced by neuropathological diagnosis, age and fixation length of the sample.

Table 1
Demographic data from final specimen selection including neuropathological group, age at time of death,sex and fixation lengths (months since date of autopsy).

Neuropathological Classification	n	Age ± SD	Male Sex (%)	Fixation Length (months) ± SD
Normal	5	69.4 ± 12.9	2 (40%)	155 ± 3,8
AD	5	75.4 ± 5.5	3 (60%)	136 ± 40.1
CVD	5	72.6 ± 13.2	4 (80%)	134 ± 39.4
AD + CVD	5	82.2 ± 5.8	1 (20%)	160 ± 3.1

2. Methods

2.1. Specimens selection

Specimens were chosen based on neuropathological findings documented at autopsy (Table 1). Coronal sections of brains were obtained from a bank of samples at the Robarts Research Institute (London, ON, Canada) that had been stored in 10% neutral buffered formalin in a research laboratory for up to 15 years following neuropathological examination. One coronal slice from the frontal lobe of each specimen was selected for imaging. The final sample selection included 20/25 scanned specimens that were grouped according to neuropathological diagnosis: 5 normal, 5 AD, 5 with features of CVD and 5 with both Alzheimer's disease and features of CVD. The CVD specimens were identified based on neuropathological findings of subcortical infarcts, microinfarcts and hypertensive vascular changes (arteriosclerosis and arteriolosclerosis). Despite the variability in length of specimen storage, the criteria used for neuropathological diagnosis has not changed substantially over the timeframe of specimen collection for this study. The remaining five specimens were excluded due to poor scan quality (presence of air bubbles, residual fixative that interfered with FLAIR imaging) that did not allow for assessment of white matter.

2.2. Brain imaging

All scans were performed at Western University's Centre for Functional and Metabolic Mapping on a 7 Tesla head-only Scanner (Siemens Magentom; Siemens Healthcare GmbH, Erlangen, Germany). An 8-channel parallel transmit/32-receive channel coil was used (Gilbert et al., 2011). Five coronal slices, one per subject, of fixed tissue from the frontal lobes of the brain were removed from formalin and immersed in Galden HT-270 perfluorinated fluid (Kurt J Lester Inc, Canada). Subjects were not grouped for scanning according to neuropathological group, and imaging for each group of 5 was conducted on separate days (Table S3). All 5 coronal sections within one session were scanned simultaneously using a custom-made stacking device consisting of Teflon bolts, with washers and spacers for securing acrylic sheets between the slices (Fig. 1). The stacking device was secured into the head coil apparatus for scanning. Structural MRI images were acquired following optimization of the imaging protocol to improve reductions in contrast due to prolonged fixation (for example extended T1 length). Imaging was acquired in the coronal orientation with the following sequences: T1-weighted images from a MP2RAGE sequence (1 mm slice thickness, TR/TE = 3000/1.72 ms, TI = 150/900 ms, flip angles = 4/5 degrees, FOV = 160 × 126 mm , in-plane resolution of 0.7 × 0.7 mm), T2-weighted images from a T2 SPACE sequence (1 mm slice thickness, TR/TE = 2500/349 ms, FOV = 160 × 120 mm, in plane resolution of 0.5 × 0.5 mm, scan repeated and averaged for increased SNR) and FLAIR images from a T2 SPACE sequence (1 mm slice thickness, TR/TE/TI = 8000/205/1600 ms, FOV = 160 × 120 mm, in-plane resolution of 0.63 × 0.63 mm). (Fig. 1A)

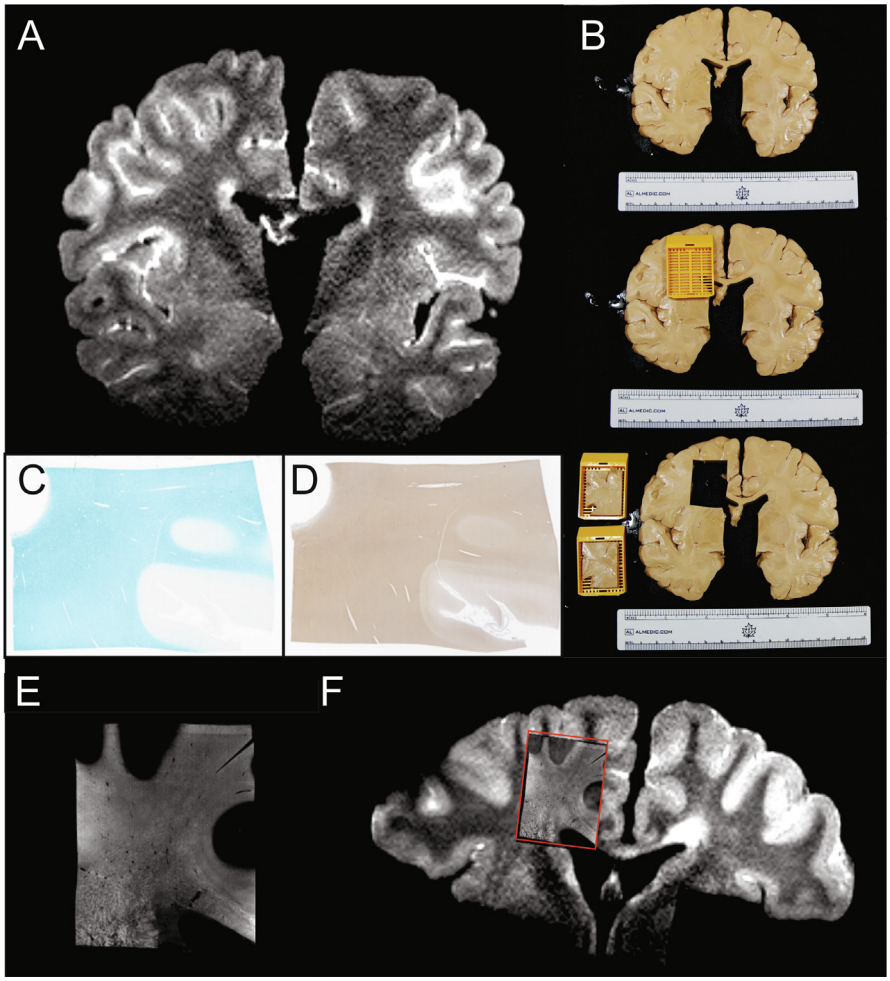

Fig. 1. Post-mortem imaging and histological co-registration workflow. A) Coronal FLAIR image of a brain section used for identification of WMH. B) Following imaging, tissue blocks were sectioned from the periventricular white matter and sent for histological analysis. Tissue blocks were stained with C) Luxol Fast Blue and D) neurofilament (Dako M762). E) Tissue sections were scanned using an Aperio slide scanner and the field-fractioned images were co-registered to the corresponding MR slices (F). (For interpretation of the references to colour in this figure legend, the reader is referred to the web version of this article.)

2.3. Tissue blocking

Fig. 1B displays the tissue blocking process where blocks were collected from the periventricular region of each coronal slice. Areas of periventricular white matter were sampled from coronal brain sections based on MRI findings with the assistance of Neuropathologists (KDL & RH). Frontal coronal sections that included all three frontal cortical regions (superior, middle and inferior) were selected. Histological blocks were obtained from brain tissue that included the periventricular white matter, subcortical white matter and cortex. One block each from the left and right hemispheres were sampled and processed for paraffin-embedding. The cortex and subcortical structures were matched to the corresponding MRI image. The imaging slice that corresponded to the surface of the tissue that was blocked was recorded for future co-registration.

2.4. Histology

Histological blocks were stained with LFB to detect myelin (Fig. 1C), neurofilament to detect axons (Fig. 1D). Tissue was paraffin embedded and sectioned at 8 μm thickness prior to staining with either hematoxylin and eosin or 0.1% Luxol Fast Blue (LFB) (Kluver, 1953) in 95% alcohol for 2 h at 60 °C. Tissue was sectioned at 4 μm and stained with neurofilament (NF) (Dako M762), 1:2000 dilution, and detected using the Dako Envision FLEX system.

2.5. Histological analysis

To quantify the LFB and NF staining: 3 images were taken at 20x magnification from both the periventricular white matter (within 0.5 mm of the ventricular lining of ependymal cells) and normal appearing white matter. Quantification was done by measuring the percent Area stained using Image J Software (Schneider et al., 2012) and averaged for the 3 images from each tissue type, generating an average proportion of area for the periventricular and normal appearing white matter for each block. A threshold for the percent area was chosen for the LFB and NF images that accurately delineated myelin and axon boundaries, respectively, and removed background staining and used for all specimens.

2.6. Digital lesion analysis

Histological slides were scanned at 20x magnification using an Aperio slide scanner. (Fig. 1 C-D). For each specimen, the surface of the coronal tissue section was matched to the corresponding MRI slice. The LFB slide was co-registered to the coronal FLAIR MRI image using deformable thin-plate spline landmark-based registration (Landmark Registration module in 3D Slicer (Kikinis et al., 2014)). (Fig. 1F) All other histological slides for each specimen were then co-registered to the LFB slide using down-sampled grayscale versions of the images and affine registration with FSL FLIRT (Jenkinson et al., 2002). Regions of interest

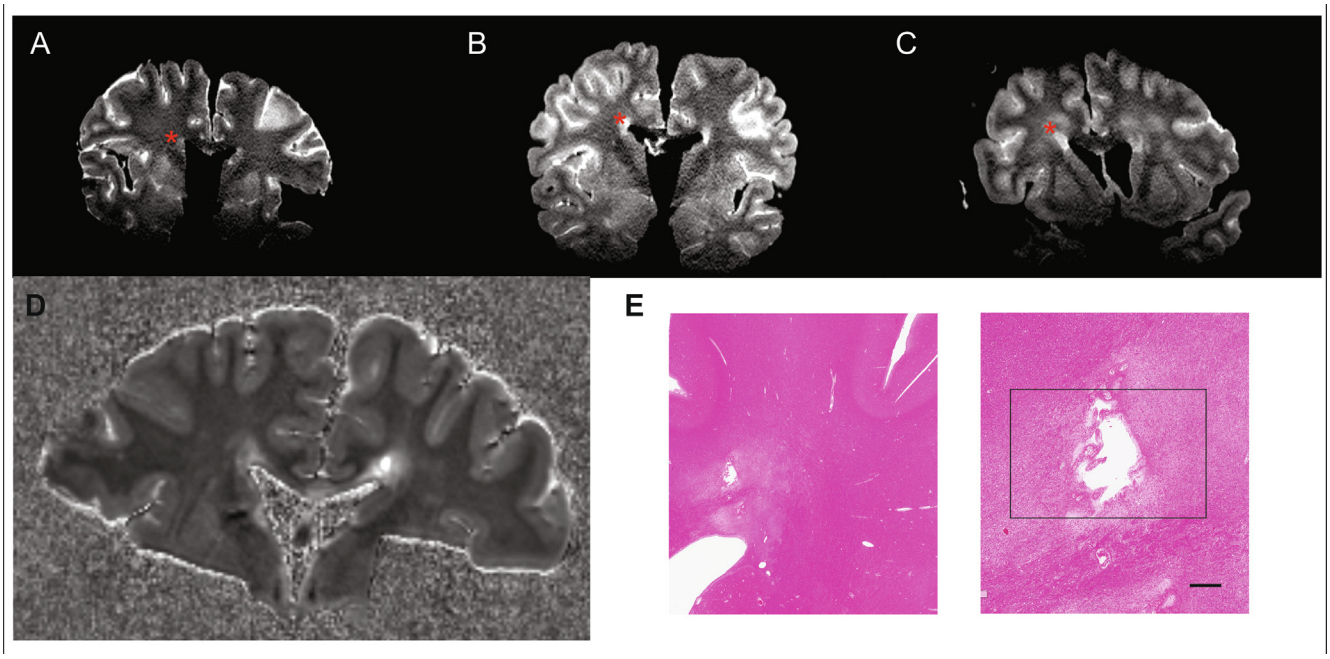

Fig. 2. Post-mortem 7 T imaging detects pvWMH of varying severity and periventricular infarcts. FLAIR sequences with A) mild amount of pvWMH, B) moderate pvWMH and C) severe pvWMH extending into the deep white matter. Lesion areas are indicated by red asterisk. D) Periventricular infarcts were identified on T1map sequences as fluid-filled cavities within pvWMH (E) H&E staining of the lesion from image D to confirm histologically the presence of periventricular infarction. Scale bar indicates 500 μm. (For interpretation of the references to colour in this figure legend, the reader is referred to the web version of this article.)

(ROI) were delineated in 3D Slicer within the boundaries of the histological section. FLAIR sequences were used to manually segment ROIs based on the inclusion of hyperintense regions that could be readily distinguished from the surrounding white matter (consistent with lesions that would be taken into account with the use of a visual rating scale such as the Fazekas scale)(Fazekas et al., 1987). . Periventricular WMH (pvWMH) were defined as hyperintense regions connected to the ependymal lining of the lateral ventricles. The normal-appearing white matter (NAWM) included subcortical white matter with a homogenous non-hyperintense FLAIR signal. Intensity values within the outlined ROI were then tabulated from the MR sequences using the Label Statistics module in 3D Slicer. Using the quantitative T1 image, fluid-filled spaces within the pvWMH ROIs were removed from intensity quantification using the Threshold Scalar Volume module in 3D Slicer. Field fraction maps, which quantify the proportion of positively-stained pixels to all pixels in a local spatial window, were generated for LFB and NF slides. This involved performing colour deconvolution to extract the colour channel of interest, and thresholding based on an adaptively-determined threshold value to segment foreground (positive pixels) and background. Field fractions were computed on the full-resolution histology images in 100x100 micron non-overlapping patches, to form maps with physical pixel dimensions of 100x100 micron representing the fraction in each patch. These maps were filtered using a Fourier domain notch filter to remove period illumination artifacts that are present due to the stitched acquisition by the slide scanner. (Fig. 1E) Code and scripts for performing image processing steps are freely available for download at https://github.com/khanlab/histmri.

2.7. Data analysis

Percent change in mean intensity values between WMH and NAWM within FLAIR ROIs was calculated using values from the FLAIR and T2 images. Spearmans's correlations between average intensity volumes within WMH and NAWM were calculated comparing T1-map, FLAIR and T2 sequences with LFB and NF. Comparisons between NAWM and WMH signal were made using Mann Whitney test. Comparisons between neuropathological groups were made using one-way Kruskal Wallis test with Dunn's post-hoc multiple comparisons test.

To perform voxel-wise predictions of FLAIR imaging intensity, linear mixed models were developed using SPSS. This allowed the inclusion of subject IDs as a random effect to control for the common effects of voxels originating from the same individual. Fixation length, diagnostic category (AD, CVD, Mixed, and normal neuropathological diagnosis), age and histological variables were included as fixed effects. FLAIR, LFB and NF values were log transformed due to their non-normal distributions. Combinations of predictors were evaluated using a stepwise regression procedure which selects for including significant predictors and removes poorly correlated predictors. Candidate regression models were compared using the standard error of residuals and the Akaike Information Criterion (AIC). The AIC is a commonly used method for comparing different models that assesses a model's relative ability to predict future values (Akaike, 1974). The final mixed model was chosen based on having the lowest AIC and lowest standard error of residuals in comparison to other models. Since log-transformed LFB and NF signal were highly correlated we retained only logLFB since it resulted in a lower AIC value. The final model included length of fixation (years), age, neuropathological diagnosis and the log-transformed LFB field fractions. A significance value of $p \leq 0.05$ was used to assess the significance of each predictor.

3. Results

Twenty specimens were retained for final study based on MR image quality and neuropathological diagnosis (Table 1). The average age of the specimens was 72.9 (SD 11.8). There was a significant difference in age between the diagnostic groups ($p = 0.0267$), with the co-morbid group being significantly older than the normal group ($p = 0.0175$). Nineteen of 20 specimens had successful co-registration between field-fractioned histological sequences and imaging sequences (Fig. 1F). To confirm the accuracy of the field-fractioned digitized images they were compared to percent area coverage of LFB and NF staining collected using brightfield microscopy. The field-fractioned LFB and NF signals were significantly correlated with the histological LFB ($r = 0.4002$, $p = 0.006$) and NF ($r = 0.5122$, $p = < 0.0001$) percent area coverage

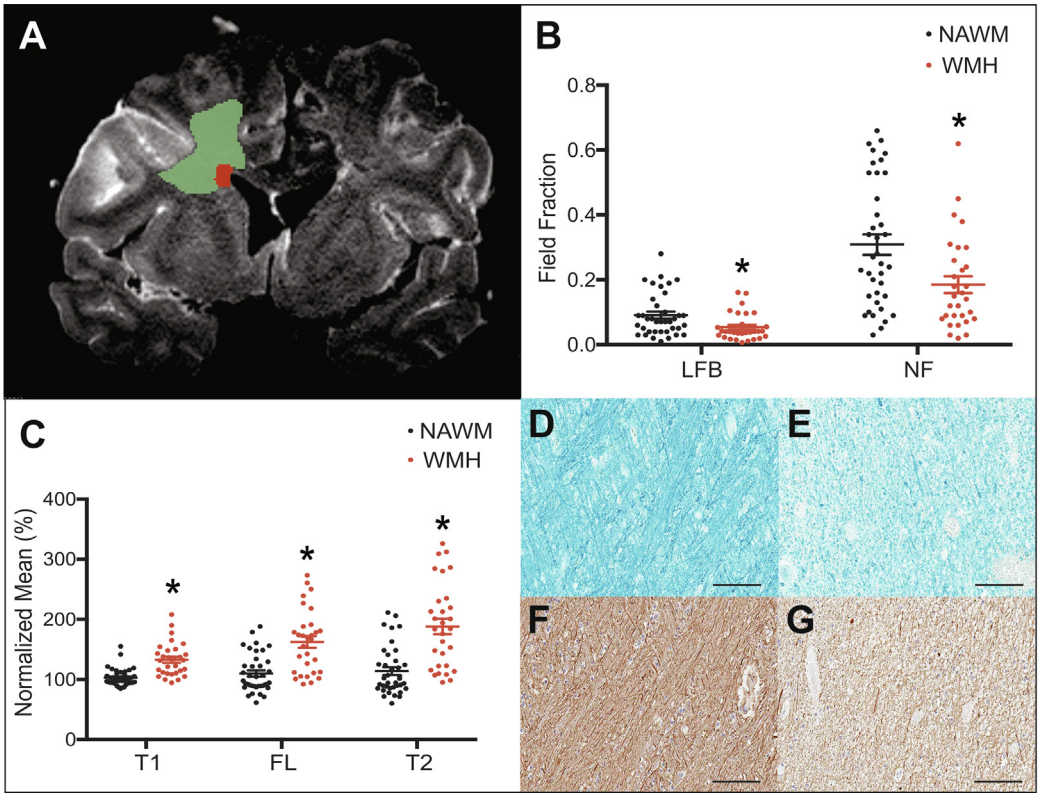

Fig. 3. Myelin and Axonal Rarefaction within WMH ROIs. A) ROIs drawn using the post-mortem FLAIR sequence to delineate pvWMH and NAWM. B) Reductions in LFB ($p = 0.0059$) and NF ($p = 0.0050$) field-fraction in pvWMH vs NAWM ROIs. C) Increase in normalized T1 ($p < 0.001$), FLAIR ($p < 0.001$) and T2 ($p < 0.001$) signal intensity in pvWMH vs NAWM. Qualitative reduction in LFB staining between D) NAWM and E) pvWMH. Qualitative reduction in neurofilament staining between F) NAWM and G) pvWMH. Scale bars indicate 100 μm. Statistics performed using SPSS software, Mann Whitney test, * indicates significance value of $p < 0.05$.

respectively.

Similar to previous reports at lower field strengths, post-mortem imaging at 7 T successfully identified pvWMH and periventricular infarcts in the fixed brain sections. Both T2 and FLAIR post-mortem sequences identified pvWMH of varying degree that ranged from a thin lining around the lateral ventricle (Fig. 2A) to larger lesions that extended into the deep subcortical white matter (Fig. 2C). In 5/20 specimens, periventricular infarcts were visible as fluid-filled cavities on T1 images in regions that were hyperintense on T2 sequences (Fig. 2D). These occurred in 3 CVD specimens, 1 AD specimen and 1 normal specimen. Evidence of infarction was confirmed histologically using H & E to rule out the presence of enlarged perivascular (Virchow-Robin) spaces which can also appear as fluid filled cavities within the white matter on T1 imaging (Fig. 2E).

To determine the ability of 7 T post-mortem MRI to distinguish tissue loss, ROIs were drawn using the FLAIR sequence as a reference to delineate normal-appearing and hyperintense white matter within the confines of the co-registered histological block (Fig. 3A). The signal intensity from NAWM and WMH ROIs was compared on digitized histology images, MR imaging sequences and microscopy acquired histological images. Quantification of the field-fractioned digitized within these ROIs displayed significant reductions in both myelin and neurofilament signal (Fig. 3B). The quantitative T1, FLAIR and T2 intensities were all significantly increased in the pvWMH ROIs in comparison to NAWM (Fig. 3C). Visible reductions in both myelin and axon content were seen qualitatively in the histological sections (Fig. 3 D-G). Next, we assessed whether intensity values from quantitative T1, FLAIR, and T2 sequences from all ROIs were significantly correlated with NF and LFB field fractions (Table 2). Within NAWM and pvWMH ROI categories, the MR values did not correlate with the histological metrics. The exception was the quantitative T1 which was significantly correlated with the NF percent area reduction in the NAWM ROIs ($p = 0.0192$).

To examine whether intensity on post-mortem MRI could accurately depict the extent of white matter rarefaction between NAWM and pvWMH, the percent loss of myelin and neurofilament signals within pvWMH was compared to corresponding increases in MR signal. This was first done in a lesion-wise manner using averages from entire ROIs. The reduction of LFB and neurofilament within pvWMH was quantified using both the percent area coverage of the microscopy acquired histological images and the field-fraction of the digitized images. The percent change of signal intensity between NAWM and pvWMH on the T2 and FLAIR sequences was not significantly correlated with the percent change of either method of histological quantification ($p < 0.05$).

Since imaging intensities were not correlated with histological signal within ROIs (pvWMH vs NAWM), linear mixed models were developed in order to assess voxel-wise predictors of FLAIR signal within NAWM and WMH. The two classifications were considered independently to determine whether the FLAIR signal was being driven by differing factors in each type of tissue. Within NAWM ROIs, the best model included the following predictors which all produced significant effect estimates: age, diagnosis of AD, CVD or mixed (both AD and CVD), fixation length, and LFB signal (Table 3B). Of these, the largest contributor to voxel-wise FLAIR intensity was LFB signal as determined by the effect estimate. NF signal was also a significant contributor to NAWM FLAIR intensity, and this effect size is presented in a separate model as it was highly correlated with the LFB signal (Table S2). Within WMH ROIs, the best model included the following predictors: age, diagnosis of AD, CVD or both (COM), fixation length and LFB signal. Of the retained predictors, the largest contributors to hyperintense voxels was the LFB voxel intensity and the diagnosis of CVD (Table 3A). NF voxel intensity did not contribute significantly to the WMH model. In

Table 2
Correlations between normalized T1, FLAIR and T2 intensities and histological quantification (% area coverage and field-fraction (FF) of digitized histological slides) within all ROIS (NAWM and pvWMH). Statistics performed using SPSS software, Spearman's correlation.

MRI Metric	LFB % area	NF % area	LFB FF	NF FF
T1 map	r = 0.5028, p = < 0.0001	r = 0.5893, p = < 0.0001	r = 0.5943, p = < 0.0001	r = 0.1802, p = 0.1415
FLAIR	r = 0.4901, p = < 0.0001	r = 0.5131, p = < 0.0001	r = 0.5288, p = < 0.0001	r = 0.2641, p = 0.0295
T2	r = 0.4998, p = < 0.0001	r = 0.5589, p = < 0.0001	r = 0.5598, p = < 0.0001	r = 0.2772, p = 0.0221

both models, a higher FLAIR signal was significantly associated with reductions in LFB, increased age, decreased length of fixation and neuropathological diagnoses of AD, CVD or both ($p < 0.001$ for all predictors). To investigate the accuracy of each model, predicted FLAIR voxel values were plotted against varying LFB field-fractions, grouped by diagnostic category (with age and fixation length held constant at 85 and 7 years, respectively) (Fig. 4). When examining the range of actual LFB values obtained, the models correctly estimate the intensity, except for the normal diagnostic group which is underestimated in the WMH model (Fig. 4A).

4. Discussion

4.1. 7 Tesla post-mortem MRI successfully identifies WMH

This work validates the use of UHF MRI as a method for studying post-mortem WMH. We report the first study to our knowledge that utilizes UHF post-mortem MRI and digitized histology for comparison of periventricular white matter lesions with histological measures. Periventricular lesions in the frontal white matter of the brain were the focus of this study since their location within long association tracts may have more specific disruption of executive functions (Bunce et al., 2010; Burton et al., 2004; Kim et al., 2015; Silbert et al., 2009). We were able to reliably detect periventricular lesions using UHF-MRI on T2 and FLAIR sequences, as is the case with UHF *in vivo* imaging and lower field strength post-mortem imaging (Murray et al., 2012; Nagara et al., 1987; Young et al., 2008). Additionally, the presence of periventricular infarcts on T1 imaging was confirmed histologically and reinforces the need for multiple sequence assessments since neither FLAIR nor T2 were able to reliably distinguish infarcts contained within a pvWMH. Post-mortem MR signals corresponded to reductions in myelin and axons as determined histologically (Table 2). Within our samples, NF and LFB staining were strongly correlated, suggesting that the pvWMH represents areas involving both myelin and axonal loss, consistent with previous radio-pathological studies of post-mortem WMH (Gouw et al., 2011; Young et al., 2008). Furthermore, the digitization of histological images resulted in quantification of LFB and NF signal that correlated to histological quantification. This supports the feasibility of combined neuroanatomical and neuroimaging approaches for the post-mortem study of clinical MR imaging features.

4.2. Lesion-wide averages of post-mortem MR are not accurate depictions of tissue loss

It is not well understood whether post-mortem WMH detected are an accurate representation of the degree of underlying white matter pathology, especially when using UHF-MRI, and whether T2 or FLAIR sequences differ in their accuracy. We report no significant difference in the signal intensity changes when comparing pvWMH to NAWM on the FLAIR and T2 sequences, suggesting that the two sequences represent WMH similarly. However, neither sequence correlated with the severity of the histological evidence of tissue loss when comparing normal appearing and hyperintense white matter ROIs in a lesion-wise manner. In addition, FLAIR and T2 intensities within pvWMH specifically did not correlate with LFB and NF percent area. Therefore, the intensity or "brightness" of the post-mortem WMH in our samples was not a reflection of the degree of myelin and axon loss when considering the average over the entire lesioned area.

Table 3
Linear mixed model results for voxel intensities within WMH ROIs and NAWM ROIs. Effect estimate represents the change in $\log_{10}$FLAIR intensity for every unit change in each predictor variable. For example, a one-year increase in age results in 5% increase in FLAIR intensity, patients with mixed AD-CVD neuropathologies have a 93% increase in FLAIR intensity compared to those with normal neuropathology, and for every 1 unit decrease in $\log_{10}$LFB the FLAIR value increases by 23%. (* indicates significance of $p < 0.001$).

A: FLAIR Voxel Intensity: WMH

	Effect Estimate (β)	Standard Error	95% CI		% change in FLAIR per 1 unit change $(10^{\beta}\text{-}1) \times 100$	95% CI	
			Lower	Upper		Lower	Upper
Intercept	0.381*	0.05	0.281	0.481			
Age (yrs)	0.021*	0.00	0.020	0.022	5.0	4.7	5.2
AD (vs. Normal)	0.183*	0.01	0.163	0.202	52.4	45.6	59.2
CVD (vs. Normal)	0.654*	0.02	0.620	0.688	350.8	316.9	387.5
Mixed (vs. Normal)	0.286*	0.01	0.267	0.304	93.2	84.9	101.4
Fixation Length (yrs)	−0.086*	0.00	−0.092	−0.081	−18.0	−19.1	−17.0
$\log_{10}$LFB	−0.111*	0.01	−0.121	−0.101	–22.6	−24.3	−20.8

B: FLAIR Voxel Intensity: NAWM

	Effect Estimate	Standard Error	95% CI		% change in FLAIR per 1 unit change	95% CI	
			Lower	Upper		Lower	Upper
Intercept	1.172*	0.020	1.132	1.211			
Age (yrs)	0.006*	0.000	0.005	0.006	1.39	1.6	1.4
AD (vs. Normal)	0.087*	0.004	0.079	0.096	22.18	19.9	24.7
CVD (vs. Normal)	0.167*	0.004	0.158	0.176	46.9	43.8	49.9
Mixed (vs. Normal)	−0.003	0.005	−0.012	−0.007	-0.7	−2.7	−1.6
Fixation Length (yrs)	−0.009*	0.000	−0.010	−0.009	−2.0	−2.3	−2.0
$\log_{10}$LFB	−0.045*	0.002	−0.047	−0.041	−9.8	−10.3	−9.0

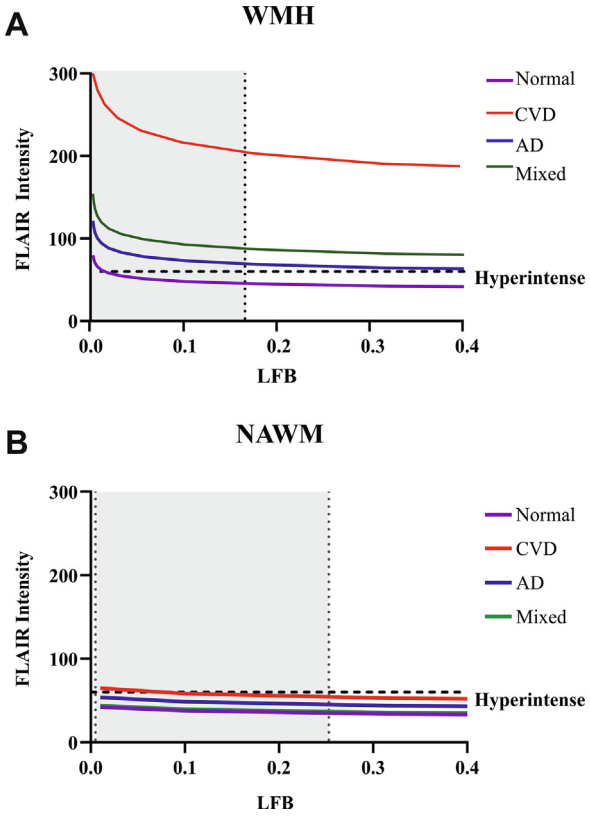

Fig. 4. Predicted FLAIR voxel intensity is driven by LFB signal and diagnostic group. Predicted voxel intensities generated from the WMH linear mixed model (A) and the NAWM linear mixed model (B). Predicted values for varying field-fractions of LFB signal are grouped by neuropathological diagnosis, with fixed values of age (85 years) and fixation (7 years). Grey shaded area indicates distribution of actual LFB values for each tissue type (only values within 2 SD of mean were included). Dashed line indicates subjective threshold where hyperintense signal becomes visually obvious on a FLAIR image.

4.3. Voxel-wise predictors of FLAIR intensity

Since ROI averages were not accurate representations of underlying histological values, and to control for other sources of variation in FLAIR intensity, we conducted a multi-variable voxel-wise analysis. The generation of mixed models allowed us to compare predictors of FLAIR signal in both normal and hyperintense white matter in a more sensitive voxel-wise approach. In both models, advanced age was associated with a significant increase in FLAIR signal suggesting that with every year increase in age there are higher intensity values. This is consistent with age-related degeneration of the white matter that would presumably affect all specimens in the study to a similar degree.

Within hyperintense voxels the main driver of FLAIR signal was the LFB field fraction and the neuropathological diagnosis of CVD. The CVD post-mortem specimens frequently contained periventricular infarcts within the periventricular WMH, which appeared as fluid filled cavities that were very hyperintense on FLAIR imaging. Despite excluding these voxels from WMH ROIs, the surrounding lesion still had more intense values, which likely contributed to the effect of CVD in the model. It also suggests that the nature of the underlying lesion, whether it be primarily myelin loss versus the presence of a complete infarction (parenchymal loss) affects the FLAIR signal throughout the hyperintense region. It is known that heterogeneity exists in the pathological correlates of WMH (Gouw et al., 2008b), and our models suggest that post-mortem UHF imaging may be able to distinguish lesions of ischemic origin (PVI).

Within the NAWM, the LFB value was once again the most significant predictor of FLAIR intensity. However, the neuropathological diagnoses remained significant predictors suggesting that there are subtle differences in the NAWM in these disease states. AD and CVD were associated with increased FLAIR signal in the NAWM compared to normal neuropathology. When looking at predicted values of FLAIR intensity (Fig. 4B), as the myelin content decreased, the signal among all diagnostic groups began to cross the threshold of what would be considered hyperintense on imaging. The predicted values within the normal subjects were more resistant to decreases in myelin signal. The subjects that were included with a normal neuropathological diagnosis in our study had very homogenous, low intensity FLAIR signal within NAWM which may have resulted in the underestimation of values in the model. Interestingly, neurofilament intensity was only a significant predictor of FLAIR signal in the NAWM, but not in the WMH. Within lesion boundaries, the LFB loss may be so profound that it overshadows the effects of axon loss, whilst in the NAWM, both contribute to FLAIR signal changes.

4.4. Underestimation of white matter rarefaction by post-mortem MRI

Previous work has indicated that post-mortem imaging underestimates the size of WMH in comparison to *in vivo* imaging (Bronge et al., 2002; Fernando et al., 2006), suggesting that the WMH visualized in this study are a conservative estimate of white matter rarefaction sustained during life. Our mixed models suggest that the subjects with the longest fixation times would have lower predicted FLAIR values, which could result in an underappreciation of hyperintense tissue and should be considered in studies where fixation length varies. Our predicted values increase within the NAWM in samples with neuropathological diagnosis of AD and CVD in comparison to the normal group, suggesting that in these samples the extent of myelin loss can extend beyond the boundaries of the FLAIR identified lesions. This is consistent with previous studies that reported *in vivo* qualitative imaging of the NAWM does not detect the full extent of white matter changes in comparison to histology or quantitative sequences (Englund et al., 1987; Muñoz Maniega et al., 2016). Additionally, WMH are considered to be a marker of small vessel disease which has been described as a global cerebral disease that extends beyond the boundaries of MRI-identified lesions (Shi and Wardlaw, 2016). Therefore, further work examining the utility of post-mortem MRI in detecting mild tissue changes associated with widespread white matter rarefaction is required.

4.5. Limitations

A limitation of this work is the restricted sample size. Future work expanding upon post-mortem imaging with a larger sample could help to further elucidate the implications of UHF imaging. Additionally, the use of histological sections that have been processed and likely subjected to some degree of tissue shrinkage and distortion introduces a potential element of error into the imaging registration. In order to minimize this issue, we utilized a non-rigid transformation model with multiple landmarks (Landmark Registration module in 3D Slicer (Kikinis et al., 2014)) for histology to imaging co-registrations. Another limitation was the lack of clinical context and *in vivo* imaging data. However, in comparison to clinical diagnoses, the neuropathological diagnoses used in this study offer greater sensitivity and specificity (Bowler et al., 1998). *In vivo* imaging would have allowed for comparisons of signal intensities in pre- and post-mortem tissue: however, it also could have introduced confounding since clinical imaging would likely have been at a lower field strength of 1.5 or 3 T. Future work comparing pre- and post-mortem imaging at 7 T would allow for the evaluation of post-mortem fixative changes.

4.6. Future directions

This work focused on pvWMH in the frontal lobe specifically; future

work will expand upon this to include deep white matter hyperintensities and other pvWMH in the other lobes of the brain. It has been suggested that the pathology underlying pvWMH may differ from focal lesions and these may show different signal abnormalities when studied with UHF MRI.

5. Conclusions

In conclusion, UHF MRI is a reliable approach to study post-mortem WMH, and combined pathological and imaging analysis of aging white matter can shed light on the global nature of the SVD. Myelin content and the presence of other cerebrovascular disease such as periventricular infarcts, are the most significant predictors of FLAIR signal in a voxel-wise manner. Alterations in myelin and axons are not limited to lesion borders and post-mortem MRI may underestimate the full extent of the pathological changes.

Funding

This work was funded by Canada First Research Excellence Fund to BrainsCAN, operating grants from the Canadian Institutes for Health Research and Canadian Consortium on Neurodegeneration and Aging to SNW, and Ontario Graduate Scholarship and Canada Graduate Scholarship to ADR.

CRediT authorship contribution statement

Austyn D. Roseborough: Conceptualization, Investigation, Formal analysis, Visualization, Writing - original draft. **Kristopher D. Langdon:** Investigation, Methodology. **Robert Hammond:** Conceptualization, Investigation. **Lauren E Cipriano:** Methodology, Visualization, Formal analysis. **Stephen H. Pasternak:** Conceptualization, Writing - review & editing. **Shawn N. Whitehead:** Conceptualization, Supervision, Resources, Writing - review & editing, Funding acquisition. **Ali R. Khan:** Conceptualization, Supervision, Resources, Writing - review & editing, Funding acquisition.

Acknowledgements

We would like to acknowledge assistance from the Department of Pathology and Laboratory Medicine, University Hospital, London and the Centre for Functional and Metabolic Mapping, Robarts Research Institute, London.

Appendix A. Supplementary data

Supplementary data to this article can be found online at https://doi.org/10.1016/j.nicl.2020.102340.

References

Akaike, H., 1974. A new look at the statistical model identification. IEEE Trans Auton. Control 19, 716–723.

Awad, I.A., Spetzler, R.F., Hodak, J.A., Awad, C.A., Carey, R., 1986. Incidental subcortical lesions identified on magnetic resonance imaging in the elderly. I. Correlation with age and cerebrovascular risk factors. Stroke 17, 1084–1089.

Black, S., Gao, F., Bilbao, J., 2009. Understanding white matter disease: Imaging-pathological correlations in vascular cognitive impairment. Stroke 40, 48–53. https://doi.org/10.1161/STROKEAHA.108.537704.

Bos, D., Wolters, F.J., L, D.S.K., Vernooij, M.W., de Wolf, F., Ikram, M.A., Hofman, A., 2018. Cerebral small vessel disease and risk of incident stroke, dementia and depression, and all-cause mortality: A systematic review and meta-analysis. Alzheimer's Dement. 1–11. https://doi.org/10.1016/j.neubiorev.2018.04.003.

Bowler, J.V., Munoz, D.G., Merskey, H., Hachinski, V., 1998. Fallacies in the pathological confirmation of the diagnosis of Alzheimer's disease. J. Neurol. Neurosurg. Psychiatry 64, 18–24.

Braffman, B., Zimmerman, R., Troianowsky, J., Gonatas, N., Hickey, W.F., Schlaepfer, W.W., 1988. Brain MR: pathologic correlation with gross and histopathology. 1. Lacunar Infarction and Virchow-Robin Spaces. Am. J. Roentgenol. 151, 559–566.

Breteler, M.M., van Swieten, J.C., Bots, M.L., Grobbee, D.E., Claus, J.J., van den Hout, J.H., van Harskamp, F., Tanghe, H.L., de Jong, P.T., van Gijn, J., 1994. Cerebral white matter lesions, vascular risk factors, and cognitive function in a population-based study: the Rotterdam Study. Neurology 44, 1246–1252.

Bronge, L., Bogdanovic, N., Wahlund, L.O., 2002. Postmortem MRI and histopathology of white matter changes in Alzheimer brains. A quantitative, comparative study 6824. Dement. Geriatr. Cogn. Disord. 13, 205–212.

Bunce, D., Anstey, K.J., Cherbuin, N., Burns, R., Christensen, H., Wen, W., Sachdev, P.S., 2010. Cognitive deficits are associated with frontal and temporal lobe white matter lesions in middle-aged adults living in the community. PLoS One 5. https://doi.org/10.1371/journal.pone.0013567.

Burton, E.J., Kenny, R.A., O'Brien, J., Stephens, S., Bradbury, M., Rowan, E., Kalaria, R., Firbank, M., Wesnes, K., Ballard, C.G., 2004. White matter hyperintensities are associated with impairment of memory, attention, and global cognitive performance in older stroke patients. Stroke 35, 1270–1275. https://doi.org/10.1161/01.STR.0000126041.99024.86.

Deary, I.J., Leaper, S.A., Murray, A.D., Staff, R.T., Whalley, L.J., 2003. Cerebral white matter abnormalities and lifetime cognitive change: a 67-year follow-up of the Scottish Mental Survey of 1932. Psychol. Aging 18, 140–148.

Debette, S., Markus, H.S., 2010. The clinical importance of white matter hyperintensities on brain magnetic resonance imaging : systematic review and. BMJ 341, 1–9. https://doi.org/10.1136/bmj.c3666.

Englund, E., Brun, A., Persson, B., 1987. Correlations between histopathologic white matter changes and proton MR relaxation times in dementia. Alzheimer Dis.Assoc. Disord.

Fazekas, F., Chawluk, J.B., Zimmerma, A., June, M., 1987. MR Signal Abnormalities at 1 . 5 T in Alzheimer ' s Dementia and Normal Aging.

Fazekas, F., Kleinert, R., Offenbacher, H., Schmidt, R., Kleinert, G., Payer, F., Radner, H., Lechner, H., 1993. Pathologic correlates of incidental MRI white matter signal hyperintensities. Neurology 43, 1683–1689.

Fernando, M.S., Brien, J.T.O., Perry, R.H., English, P., Forster, G., Mcmeekin, W., Slade, J. Y., Golkhar, A., Matthews, F.E., Barber, R., Kalaria, R.N., Ince, P.G., Barber, R., Kalaria, R.N., Neuropathology, P.G.I., Neurobiology, A., 2004. Comparison of the pathology of cerebral white matter with post-mortem magnetic resonance imaging (MRI) in the elderly brain 385–395. https://doi.org/10.1111/j.1365-2990.2004.00550.x.

Fernando, M.S., Simpson, J.E., Matthews, F., Brayne, C., Lewis, C.E., Barber, R., Kalaria, R.N., Forster, G., Esteves, F., Wharton, S.B., Shaw, P.J., Brien, J.T.O., 2006. White Matter Lesions in an Unselected Cohort of the Elderly Molecular Pathology Suggests Origin From Chronic Hypoperfusion Injury " I Histologic studies in Binswanger disease and AD show. Stroke 37, 1391–1398. https://doi.org/10.1161/01.STR.0000221308.94473.14.

Gilbert, K.M., Curtis, A.T., Gati, J.S., Klassen, L.M., Menon, R.S., 2011. A radiofrequency coil to facilitate B shimming and parallel imaging acceleration in three dimensions at 7 T. NMR Biomed. 24, 815–823. https://doi.org/doi:10.1002/nbm.1627.

Gouw, A.A., Seewann, A., van der Flier, W.M., Barkhof, F., Rozemuller, A.M., Scheltens, P., Geurts, J.J.G., 2011. Heterogeneity of small vessel disease: a systematic review of MRI and histopathology correlations. J. Neurol. Neurosurg. Psychiatry 82, 126–135. https://doi.org/10.1136/jnnp.2009.204685.

Gouw, A.A., Seewann, A., Vrenken, H., Flier, W.M. Van Der, Rozemuller, J.M., Barkhof, F., Scheltens, P., Geurts, J.J.G., 2008a. Heterogeneity of white matter hyperintensities in Alzheimer ' s disease : post-mortem quantitative MRI and neuropathology. Brain 131, 3286–3298. https://doi.org/10.1093/brain/awn265.

Gouw, A.A., Seewann, A., Vrenken, H., van der Flier, W.M., Rozemuller, J.M., Barkhof, F., Scheltens, P., Geurts, J.J.G., 2008b. Heterogeneity of white matter hyperintensities in Alzheimer's disease: post-mortem quantitative MRI and neuropathology. Brain 131, 3286–3298. https://doi.org/https://dx.doi.org/10.1093/brain/awn265.

Grafton, S.T., Sumi, S.M., Stimac, G.K., Alvord Jr., E.C., Shaw, C.M., Nochlin, D., 1991. Comparison of postmortem magnetic resonance imaging and neuropathologic findings in the cerebral white matter 9460. Arch Neurol. 48, 293–298.

Grinberg, L., Junior, E., Valotta de Silva, A., Emidio da Silva, R., Sato, J., Dionizio dos Santos, D., Pacheco, S.D.P., Renata, F., Leite, R., Pasqualucci, C., Teipel, S.J., Flatz, W.H., Brazilian Aging Study Group, Heinsen, H., 2009. Improved detection of incipient vascular changes by a biotechnological platform combining post mortem MRI in situ with neuropathology. J. Neurol. Sci. 283, 2–8. https://doi.org/10.1016/j.jns.2009.02.327.

Jacobs, H.I.L., Visser, P.J., Van Boxtel, M.P.J., Frisoni, G.B., Tsolaki, M., Papapostolou, P., Nobili, F., Wahlund, L.O., Minthon, L., Frölich, L., Hampel, H., Soininen, H., van de Pol, L., Scheltens, P., Tan, F.E.S., Jolles, J., Verhey, F.R.J., 2012. The association between white matter hyperintensities and executive decline in mild cognitive impairment is network dependent. Neurobiol. Aging 33, 201.e1–201.e8. https://doi.org/10.1016/j.neurobiolaging.2010.07.015.

Jenkinson, M., Bannister, P., Brady, M., Smith, S., 2002. Improved optimization for the robust and accurate linear registration and motion correction of brain images. Neuroimage 17, 825–841.

Kikinis, R., Pieper, S.D., Vosburgh, K.G., 2014. 3D Slicer: A Platform for Subject-Specific Image Analysis, Visualization, and Clinical Support, in: Jolesz, F.A. (Ed.), Intraoperative Imaging and Image-Guided Therapy. Springer New York, New York, NY, pp. 277–289. https://doi.org/10.1007/978-1-4614-7657-3_19.

Kim, H.J., Im, K., Kwon, H., Lee, J.-M., Kim, C., Kim, Y.J., Jung, N.-Y., Cho, H., Ye, B.S., Noh, Y., Kim, G.H., Ko, E.-D., Kim, J.S., Choe, Y.S., Lee, K.H., Kim, S.T., Lee, J.H., Ewers, M., Weiner, M.W., Na, D.L., Seo, S.W., 2015. Clinical effect of white matter network disruption related to amyloid and small vessel disease. Neurology 85, 63–70. https://doi.org/10.1212/WNL.0000000000001705.

Kluver, Barrera, 1953. A method for the combined staining of cells and fibers in the nervous system. J. Neuropathol. Exp. Neurol. 12, 400–403. https://doi.org/10.1097/00005072-195312040-00008.

Lee, S., Viqar, F., Zimmerman, M.E., Narkhede, A., Tosto, G., Benzinger, T.L.S., Marcus, D. S., Fagan, A.M., Goate, A., Fox, N.C., Cairns, N.J., Holtzman, D.M., Buckles, V., Ghetti, B., McDade, E., Martins, R.N., Saykin, A.J., Masters, C.L., Ringman, J.M., Ryan, N.S., Förster, S., Laske, C., Schofield, P.R., Sperling, R.A., Salloway, S., Correia, S., Jack, C., Weiner, M., Bateman, R.J., Morris, J.C., Mayeux, R., Brickman, A.M., Dominantly Inherited Alzheimer Network, 2016. White matter hyperintensities are a core feature of Alzheimer's disease: Evidence from the dominantly inherited Alzheimer network. Ann. Neurol. 79, 929–39. https://doi.org/10.1002/ana.24647.

Muñoz Maniega, S., Chappell, F.M., Valdés Hernández, M.C., Armitage, P.A., Makin, S.D., Heye, A.K., Thrippleton, M.J., Sakka, E., Shuler, K., Dennis, M.S., Wardlaw, J.M., 2016. Integrity of normal-appearing white matter: Influence of age, visible lesion burden and hypertension in patients with small-vessel disease. J. Cereb. Blood Flow Metab. 37, 644–656. https://doi.org/10.1177/0271678X16635657.

Murray, M.E., Vemuri, P., Preboske, G.M., Matthew, C., Schweitzer, K.J., Parisi, J.E., Jr, C.R.J., Dickson, D.W., 2012. A Quantitative Postmortem MRI Design Sensitive to White Matter Hyperintensity and their Relationship with Underlying Pathology. J Neuropath Exp Neurol 71, 1113–1122. https://doi.org/10.1097/NEN.0b013e318277387e.A.

Nagara, H., Inoue, T., Koga, T., Kitaguchi, T., Tateishi, J., Goto, I., 1987. Formalin fixed brains are useful for magnetic resonance imaging (MRI) study 67–77.

Scheltens, P., Barkhof, F., Leys, D., Wolters, E.C., 1995. Histopathologic correlates of white-matter changes on MRI in Alzheimer ' s disease and normal.

Schneider, C.A., Rasband, W.S., Eliceiri, K.W., 2012. NIH Image to ImageJ: 25 years of image analysis. Nat. Methods 9, 671–675.

Shi, Y., Wardlaw, J.M., 2016. Update on cerebral small vessel disease: a dynamic whole-brain disease. Stroke Vasc. Neurol. 1, 83–92. https://doi.org/10.1136/svn-2016-000035.

Silbert, L.C., Howieson, D.B., Dodge, H., Kaye, J.A., 2009. Cognitive impairment risk: white matter hyperintensity progression matters. Neurology 73, 120–125. https://doi.org/10.1212/WNL.0b013e3181ad53fd.

Swardfager, W., Yu, D., Ramirez, J., Cogo-moreira, H., Szilagyi, G., Holmes, M.F., Scott, C.J.M., Scola, G., Chan, P.C., Chen, J., Chan, P., Sahlas, D.J., Herrmann, N., Lanct, K. L., Andreazza, A.C., Pettersen, J.A., Black, S.E., 2017. Peripheral inflammatory markers indicate microstructural damage within periventricular white matter hyperintensities in Alzheimer ' s disease : A preliminary report 7, 56–60. https://doi.org/10.1016/j.dadm.2016.12.011.

van den Hauwe, L., Parizel, P.M., Martin, J.J., Cras, P., De Deyn, P., De Schepper, A.M.A., 1995. Postmortem MRI of the brain with neuropathological correlation 343–349 parallel imaging acceleration.

Wardlaw, J.M., Smith, E.E., Biessels, G.J., Cordonnier, C., Fazekas, F., Frayne, R., Lindley, R.I., O'Brien, J.T., Barkhof, F., Benavente, O.R., Black, S.E., Brayne, C., Breteler, M., Chabriat, H., DeCarli, C., de Leeuw, F.E., Doubal, F., Duering, M., Fox, N.C., Greenberg, S., Hachinski, V., Kilimann, I., Mok, V., Oostenbrugge, R. Van, Pantoni, L., Speck, O., Stephan, B.C.M., Teipel, S., Viswanathan, A., Werring, D., Chen, C., Smith, C., van Buchem, M., Norrving, B., Gorelick, P.B., Dichgans, M., Brien, J.T.O., Doubal, F., Duering, M., Fox, N.C., Greenberg, S., Hachinski, V., Kilimann, I., Mok, V., van Oostenbrugge, R.J., Pantoni, L., Speck, O., Stephan, B.C.M., Teipel, S., Viswanathan, A., Werring, D., Chen, C., Smith, C., 2013. Neuroimaging standards for research into small vessel disease and its contribution to ageing and neurodegeneration. Lancet Neurol. 12, 822–838. https://doi.org/10.1016/S1474-4422(13)70124-8.

Wen, W., Sachdev, P.S., Li, J.J., Chen, X., Anstey, K.J., 2009. White matter hyperintensities in the forties: Their prevalence and topography in an epidemiological sample aged 44–48. Hum. Brain Mapp. 30, 1155–1167. https://doi.org/10.1002/hbm.20586.

Wen, W., Sachdev, P.S., Li, J.J., Chen, X., Anstey, K.J., 2008. White matter hyperintensities in the forties: Their prevalence and topography in an epidemiological sample aged 44-48. Hum.Brain Mapp.

Young, V.G., Halliday, G.M., Kril, J.J., 2008. Neuropathologic correlates of white matter hyperintensities. Neurology 71, 804–811. https://doi.org/10.1212/01.wnl.0000319691.50117.54.